

Article

CsPbBr₃ Nanocrystals-Based Polymer Nanocomposite Films: Effect of Polymer on Spectroscopic Properties and Moisture Tolerance

Elisabetta Fanizza ^{1,2,*}, Roberto Schingo ¹, Annamaria Panniello ², Angelica Maria Lanza ¹, Nicoletta Depalo ², Angela Agostiano ^{1,2}, Maria Lucia Curri ^{1,2} and Marinella Striccoli ^{2,*}

¹ Dipartimento di Chimica, Università Degli Studi di Bari, Via Orabona 4, 70125 Bari, Italy; schingo.roberto@gmail.com (R.S.); a.lanza5@studenti.uniba.it (A.M.L.); angela.agostiano@uniba.it (A.A.); marialucia.curri@uniba.it (M.L.C.)

² CNR-IPCF, SS Bari, Via Orabona 4, 70125 Bari, Italy; a.panniello@ba.ipcf.cnr.it (A.P.); n.depalo@ba.ipcf.cnr.it (N.D.)

* Correspondence: elisabetta.fanizza@uniba.it (E.F.); m.striccoli@ba.ipcf.cnr.it (M.S.)

Received: 2 December 2020; Accepted: 18 December 2020; Published: 20 December 2020



Abstract: Metal halide perovskites nanocrystals (NCs) represent an emerging class of materials that find increasing application in optoelectronic and photovoltaic devices, thanks to their intriguing optical properties, including high absorption coefficient, high fluorescence quantum yield (PL QY) and fast charge carrier separation. However, their opening to market is still hindered by their limited reliability, due to an intrinsic structural instability and degradation of their photophysical properties upon air, moisture, and light exposure. The incorporation of perovskite NCs in polymer matrix can limit some of the NC instability issues, with advantages in film processability, device fabrication and mechanical performance, being also useful for fundamental studies. In this regard, here, nanocomposites based on polymethylmethacrylate or polystyrene embedding all-inorganic CsPbBr₃ NCs have been prepared and processed in the form of flexible free-standing films. A systematic spectrofluorimetric study, comprising steady state photoluminescence (PL), PL quantum yield (QY) and PL decay of the free-standing films before and after exposure to relative humidity condition (RH% 85%, at 25 °C) is performed and discussed. Phase segregation phenomena, changes in NC passivation and recombination dynamics are evaluated as a function of polymer loading and its molecular structure and finally the efficacy of the polymer as moisture barrier investigated.

Keywords: CsPbBr₃ NCs; polymer nanocomposites; steady state emission; time resolved spectra; recombination dynamics

1. Introduction

Metal halide perovskites, including both hybrid organic–inorganic (HOIPs) and all-inorganic cesium-based perovskites (IPs), have shown great potential for next generation optoelectronic devices thanks to their outstanding photophysical properties [1,2]. Broad absorption, composition and size dependent optical properties, narrow emission line width (70–140 meV), high (40–90%) photoluminescence quantum yield (PL QY) [2–4], fast charge separation, and long carrier lifetime, together with low cost and easy processability, are some of the features of these emerging materials that make them attractive as active components in third-generation solar cells [5,6] and light emitting devices [7].

While the defect tolerant nature of perovskite is the major enabling factor for highly efficient perovskite photovoltaics and for the bright photoluminescence, the easy ion-migration phenomenon, and the low energy formation [8] stand as potential threat against stability [9]. In fact,

the commercialization of optoelectronic and photovoltaic devices based on perovskites is still in its early stages due to their poor reliability, short lifespan, and quick deterioration of the active materials. Long-term instability issues, indeed, include both a limited structural/intrinsic stability of perovskites and their heavy deterioration under external environmental stresses such as heat, light, humidity, and oxygen [10,11]. HOIPs suffer from low intrinsic or thermodynamic stability due to the high mobility of halide and organic ions. Organic cations are volatile and hygroscopic; thus, hydrate perovskite intermediates and degradation products can be easily formed from reactions catalyzed by water in humid air. The organic cations are also protonated, which makes them easily reacting with superoxide, formed under light and oxygen exposure [8,12,13], thus undergoing deterioration. Conversely, IP materials featuring large inorganic cesium ions instead of organic cations [14] may represent viable alternatives, showing superior stability compared to HOIPs. Cesium ions indeed provide an improved tolerance to oxygen under light exposure, due to lack of protonated moieties [13], and, in general, convey an inherently more rigid crystal structure, enabling a higher resistance to the electrochemical changes under external stimuli [8].

In the field of IP materials, colloidal perovskite nanocrystals (NCs) featuring low dimensionality and good colloidal dispersibility in organic solvents, thanks to native amphiphilic ligands passivating their surface, have shown superior long-term stability with respect to bulk materials [15]. The presence of the hydrophobic ligand shell, even though dynamically adsorbing and desorbing from the IP NCs surface, improves materials tolerance to humidity, limiting moisture diffusion. In addition, their colloidal nature and large surface area, due to low dimensions, offer the possibility of implementing a wide range of solution phase IP surface functionalization strategies alternatives to the use of thin films protecting coating. Several approaches based on IP NC surface engineering with hydrophobic water-resistant interfaces have been developed [16,17] to preserve the structure of IP NCs and render them resistant to moisture and air. IP NCs have been surface-functionalized with specific ligands [18–20] such as fluorocarbon agents [18], inorganic matrixes [21], polymers [15,16,22–25], biopolymers [26] or superhydrophobic porous polymer framework [27]. Other approaches are based on the coating of IP NCs with an inorganic oxide layer [28,29] or on their inclusion in a hydrophilic network [30,31] which, concomitantly, provide moisture resistance and act as a physical barrier, preserving the IP NCs properties. More recently, the phase transformation of IP NCs into 2D/3D heterostructures has been found to offer a great advantage to IP NC stability [32,33].

In this scenario, the formation of polymer nanocomposites (PNC) based on IP NCs dispersion in a polymer matrix, such as poly (methyl methacrylate) (PMMA), polystyrene (PS), polycarbonate, acrylonitrile, butadiene, polyvinyl chloride, and styrene, characterized by a relatively low water and oxygen permeability, has shown promising results to solve some of the IP NC instability issues, meeting also the requirements for device fabrication processing and mechanical performance [34]. Their efficacy as moisture barrier has been investigated exploring different PNC fabrication strategies, either *ex situ* or *in situ* [15,16,22–25]. Although the *in situ* approach has resulted more advantageous, being less time-consuming and more sustainable, since it relies on one step procedure and requires a relatively low solvent volume, the use of polymerization initiators and thermal- or light-catalyzed polymerization processes, needed for PNC preparation, may induce IP NCs deterioration. In fact, such processes have been considered responsible for the loss of stability and the degradation of the optical properties of IP NCs embedded, for example, in styrene-based polymer [23]. Conversely, the *ex situ* approach provides a straightforward fabrication procedure of PNC, even though affinity between polymer matrix and IP NC surface chemistry and wettability are critical since they drive the arrangement of IP NCs within the polymer matrix, enabling their effective dispersion or conversely allowing the formation of phase segregated nanostructures, and thus ultimately affecting the optical properties.

Widely applied in many technological fields and for inorganic nanocrystals based nanocomposites [35], both PMMA and PS represent a viable choice as polymeric matrices for IP NCs, since they are characterized by a relatively low water diffusion constant (nearly 10^{-8} cm²/s) [36],

high moisture resistance and low oxygen permeability (water permeability coefficients 1.7 and 0.8–3.9 g mm/m² day, percentage of water absorption of 0.1–2 and 0.05–0.3 and oxygen permeability coefficient of 5.8–6.7 and 98.5–171 cm³ mm/m² day atm for PMMA and PS, respectively) [25,37,38] that are stringent requirements for their use as barrier to protect the IP NCs from moisture and air exposure. In addition, both the polymers are optically transparent in the visible region, thus not interfering with the emission and absorption characteristics of IP NCs.

Here, commercial high molecular weight PMMA and PS polymers are tested as matrices to embed amphiphilic ligand capped green-emitting CsPbBr₃ NCs. The PNC blends, processed in free-standing films, are characterized by steady-state fluorescence, decay lifetime, PL QY (i) to evaluate the effect of the polymer matrix and its load in the stabilization of the CsPbBr₃ NCs and (ii) to investigate the behavior of the PNC compared to bare NC thin films against the exposure to air with relative high humidity and room temperature conditions. PL properties are indeed peculiar signatures of the IP NCs, effective in monitoring any intrinsic structural and morphological changes, modifications of NC passivation, NC segregation and/or aggregation phenomena. Such features are essential in view of the IP NCs integration in optoelectronic devices where charge carrier dynamics and emission properties determine the device performances and durability. The results of the study allow to depict the distinct degradation process for bare NC thin film compared to free-standing PNC film exposed to moisture. The polymers are definitely able to limit recrystallization phenomena and size increase of NCs, even though their sensitivity to humidity is strongly dependent on the amount of polymer in the PNC and, accordingly, on its moisture up taking and swelling properties.

2. Materials and Methods

Materials: PbBr₂ (98%), octadecene (ODE, 90%), oleic acid (OA, 90%), oleylamine (OAM, 70%), Cs₂CO₃ (99.9%), toluene (anhydrous), poly (methylmethacrylate) (PMMA, 996 kDa), and polystyrene (PS, 280 kDa) were purchased from Sigma-Aldrich. All the materials were used without any further purification.

Methods: Solution-based synthesis of colloidal CsPbBr₃ NCs. The synthesis of CsPbBr₃ NCs was carried out following the procedure reported in Fanizza et al. [11], whereby 0.4 mmol of PbBr₂, 10 mL of ODE (40 mM), 3.0 mmol of OA (0.3 M) and 3.0 mmol of fresh OAM (0.3 M) were poured in a three-necked flask and put under vacuum at 80 °C for 1 h, before raising the temperature up to 150 °C under nitrogen flux for 30 min. The cesium precursor was prepared in a second three necked flask, by dispersing 0.4 mmol of Cs₂CO₃ in 5 mL of ODE ([Cs⁺] = 80 mM) with 2.5 mmol of OA (0.5 mM). After a first step under vacuum at 100 °C for 1 h, the mixture was heated up to 150 °C under N₂ atmosphere to completely decompose the Cs₂CO₃ in Cs-oleate (pale yellow solution). Then, 0.8 mL of Cs-oleate (0.06 mmol) was injected at 140 °C in the mixture containing the lead/bromine precursors, it turns into an intense yellow-green color, and was suddenly cooled down at room temperature by immersion in ice bath. The NCs were collected by centrifugation at 750× g for 1 h at 10 °C without non-solvent addition and the pellet was finally redispersed in 6 mL of anhydrous toluene. For NC thin film preparation, 50 μL of NC solution were spun onto a quartz 1 × 1 cm² substrate (800 rpm for 30 s), and then thermally treated at 40 °C for 5 min to allow the solvent evaporation.

PMMA- and PS-based freestanding film fabrication: PMMA polymer solutions were prepared by dissolving 40, 80, or 140 mg of PMMA into 2.8 mL of anhydrous toluene. Then, 200 μL of the as-synthesized CsPbBr₃ NCs at 0.8 μM, corresponding to 0.4 mmol, were finally added and the blend was let stirring for three hours. As shown in Figure S2, the PNC blend was poured in a Teflon Petri dish, used to mold the freestanding film, then the solvent was let to evaporate upon gentle heating. Bubbles and solvent entrapped within the film were further removed by vacuum treatment, prior to film detachment from the substrate. Freestanding films were used for spectroscopic investigation and post preparative moisture exposure treatments. As a comparison, 80 mg PS free-standing film were also prepared by using the same procedure.

Moisture/air stability experiment: A saturate salt solution was used to set humidity condition that remains quite stable by the time. Humidity range depends on the salt nature, hygroscopicity and temperature condition. Here, KNO_3 was selected, characterized by harsh moisture condition with a relative humidity (RH%) of nearly 85–90% at 25 °C. CsPbBr_3 NC thin film and PMMA- and PS-based freestanding films were put in a closed chamber, formed by a falcon tube, under controlled temperature (25 °C) and moisture, set by the KNO_3 salt saturated water. The salt was put at the bottom of the tube and separated by a porous seal from the film. Relative humidity value was measured using a hygrometer.

Characterization techniques: Cary 5000 (Varian) UV/Vis/NIR was used to perform the UV-Vis absorption characterization. The spectra were recorded by solvent diluting the NC solution 1:100 ($\epsilon \sim 10^7 \text{ cm}^{-1} \text{ M}^{-1}$). All fluorescence measurements were performed on solid films. A HORIBA Jobin-Yvon Fluorolog 3 spectrofluorimeter, equipped with double grating excitation and emission monochromators, was used to record photoluminescence spectra (PL). Time resolved photoluminescence (TRPL) measurements were performed by Time-Correlated Single Photon Counting (TCSPC) technique with a FluoroHub (by HORIBA Jobin-Yvon). Excitation at 375 nm by means of a picosecond laser diode (NanoLED 375L) and a pulse length of 80 ps at a 1 MHz repetition rate was carried out. The PL signals were dispersed by a double grating monochromator and detected by a picosecond photon counter (TBX Photon Detection Module, HORIBA Jobin-Yvon). The time resolution of the experimental set up was ~ 200 ps. Absolute quantum yields value and 1931 CIE colour point measurements were obtained by means of a “Quanta-phi” integrating sphere coated with Spectralons® and mounted in the optical path of the spectrofluorometer, using as an excitation source a 450 W xenon lamp coupled with a double-grating monochromator. The transmission electron microscopy (TEM) analysis was carried out using a JEOL JEM1011 microscope, operating at an accelerating voltage of 100 kV and equipped with a W electron source and a CCD high resolution camera. Samples were prepared by dipping a carbon-coated copper grid into the NC solution at 1:100 dilution with anhydrous toluene or by spin coating the nanocomposite directly on the TEM grid. Statistical analysis of the size of the samples was carried out by using the freeware image analysis program Image J. The percentage relative standard deviation ($\sigma\%$) was calculated for each sample, to estimate the NC size distribution, expressed as a percentage, based on the distribution of size with respect to the average value. Spectroscopic and morphologic characterizations were performed at room temperature.

3. Results

Oleic acid (OA)- and oleylamine (OAM)-capped colloidal CsPbBr_3 NCs were synthesized [11] by Cs-oleate injection ($T_{\text{injection}} = 140$ °C) in the reaction mixture containing already decomposed PbBr_2 in the presence of OA and OAM, followed by a fast cooling. TEM micrograph (Figure 1a) of the purified NCs shows square-shaped nanostructures, ascribable to nanocubes, with an average edge length of nearly 8 nm, above the confinement regime for CsPbBr_3 (exciton Bohr radius 7 nm [34]), and with a low percentage of polydispersity ($\sigma\%$) of nearly 12% (Figure S1), characteristic of narrow size distributed NCs.

The spectroscopic investigation was accomplished by recording UV-Vis absorption spectrum of CsPbBr_3 NCs in anhydrous toluene, while emission spectra of NC thin film prepared by spinning the colloidal solution on quartz slides have been acquired. Due to the high extinction coefficient [39] of the CsPbBr_3 NCs sample, a high dilution would have been required to attain an optical density suitable for PL investigation in solution (<0.1). However, due to the demonstrated CsPbBr_3 NCs lability in solvent [11,25], PL investigation of highly diluted NC solutions may endanger their structural integrity.

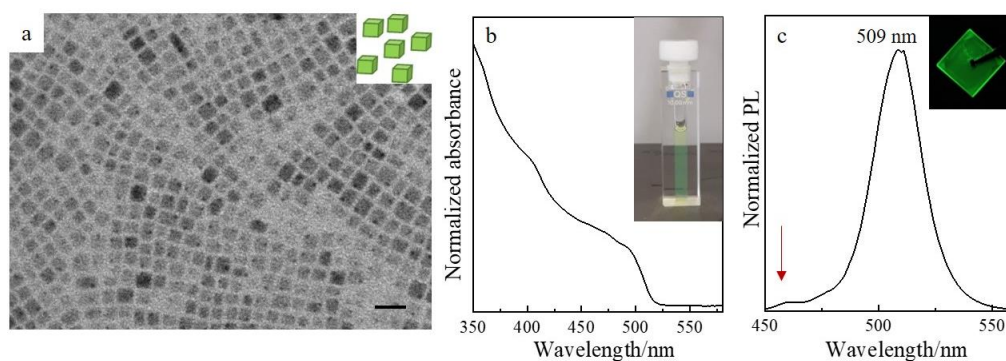


Figure 1. Transmission electron micrograph (a, scale bar 20 nm), UV-Vis absorbance (b) and photoluminescence (c) spectra of organic-capped CsPbBr₃ NCs in toluene solution (b) and spin coated on quartz slide (c). Pictures of the colloidal CsPbBr₃ NCs solution under solar light illumination and of CsPbBr₃ NC thin film on quartz under 365 nm UV- lamp illumination are reported as inset in panel b and c, respectively.

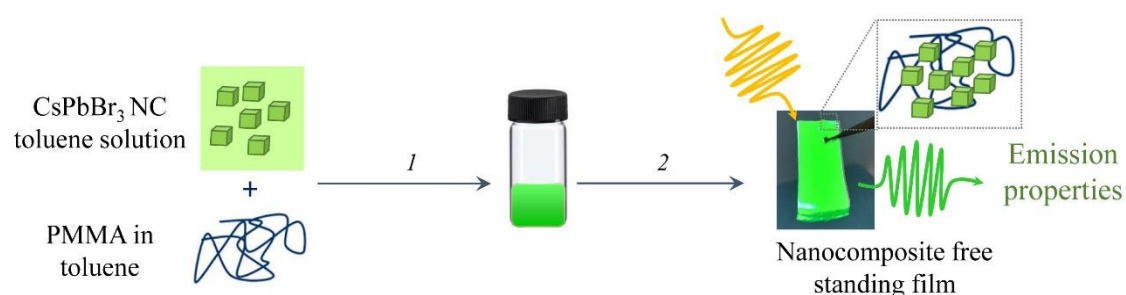
In Figure 1b the UV-V is absorption spectrum of CsPbBr₃ NCs solution shows the characteristic line profile [40] of this material with a first exciton transition signal at 491 nm (2.53 eV) and an energy gap, determined from Tauc plot, of 2.4 eV (data not shown), in agreement with the value expected for not quantum confined CsPbBr₃. The NC thin film (Figure 1c) shows an emission band centered at 509 nm (2.43 eV), similar to what reported for NCs of comparable size [2,40,41], a narrow full width at half maximum (FWHM) of 115 meV that indicates a PL emission mainly arising from the exciton recombination, and a high PL QY of nearly 55%. The weak emission band at higher energy (red arrow in Figure 1c) can be reasonably ascribed to smaller NCs side-products or 2D platelets, generated during the synthesis [11,42]. In fact, shape purity represents one of the main concerns of the synthesis of these nanomaterials, thus making challenging the fabrication of a single type of nanostructure [43].

Commercial high molecular weight PMMA (996 kDa) was investigated as polymer matrix to embed, by means of an *ex situ* approach, organic-capped CsPbBr₃ NCs, to protect them from oxygen and moisture environmental stress. Largely used in polymer-based technologies, PMMA is characterized by a partial moisture resistance and poor oxygen permeability (water permeability coefficients 1.7 g mm/m² day, percentage of water absorption of 0.1–2 and oxygen permeability of 5.8–6.7 cm³ mm/m² day atm) [25].

Thanks to its relatively good dispersibility in organic solvent, PMMA was dispersed in toluene solution and mixed with the as-synthesized CsPbBr₃ NCs in anhydrous toluene and the resulting PNC dispersion was processed in free-standing films, allowing solvent evaporation (Scheme 1), for fundamental spectroscopic investigation [44]. Compared to substrate-deposited thin films, the free-standing counterparts enable to rule out the influence of the geometry/properties of the underneath substrate in the study of the PNC properties.

Anhydrous toluene represents a convenient common solvent for the preparation of the NC and polymer blend, since it is suited to effectively disperse organic-capped NCs and easily dissolves the PMMA, due to its limited hydrophobicity. Its relatively low index polarity (2.2) preserves the CsPbBr₃ NCs, characterized by ionic nature and labile anchoring of amphiphilic passivating ligands, from decomposition, which, instead, usually occurs in more polar solvents. The effect of polymer load was investigated by dissolving 40, 80 and 140 mg of PMMA in toluene (2.8 mL) while a fixed amount of CsPbBr₃ NCs solution (200 µL of 0.8 µM colloidal solution corresponding to 0.4 mmol of CsPbBr₃ NCs) was added.

The suited volume of the PNC toluene dispersion (3 mL) was experimentally determined, in order to ensure the complete mold filling and the formation of a homogeneous and easily detachable film of about 5 cm in diameter (Figure S2 and Figure 2a).



Scheme 1. *Ex situ* preparation of the nanocomposite (PNC, *step 1*) by mixing anhydrous toluene solution of CsPbBr₃ nanocrystals (NCs) and toluene dispersed PMMA; PNC fabrication in free-standing film by solvent evaporation (*step 2*) for the following emission properties characterization. Sketch of the PNC free standing film showing CsPbBr₃ NCs embedded in a polymer matrix.

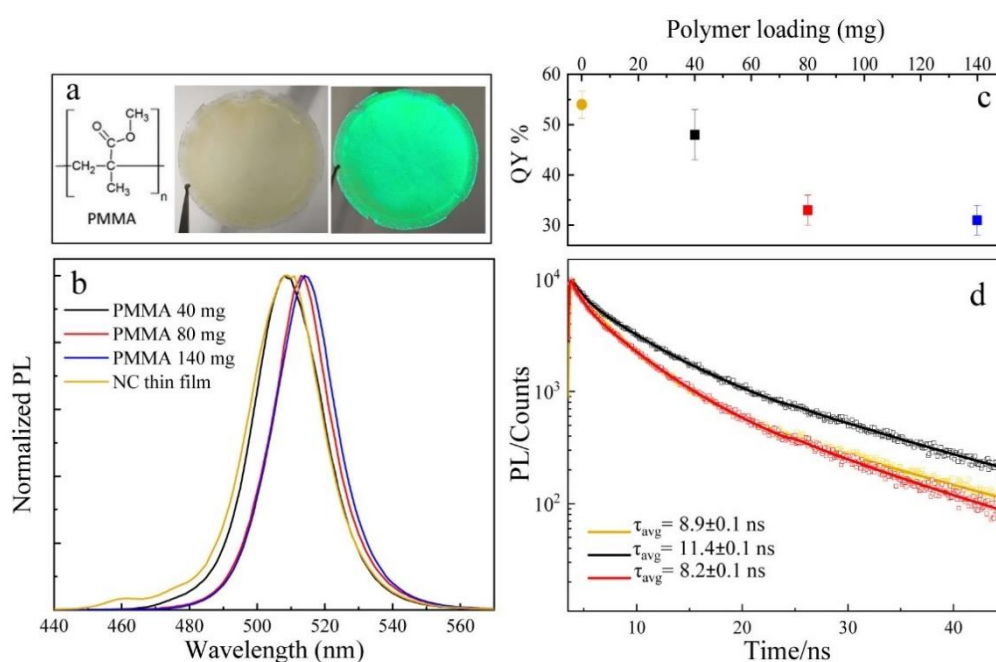


Figure 2. (a) Pictures of the free-standing nanocomposite film (80 mg PMMA) under white (left) and UV light (right) along with the molecular structure of the PMMA. (b) Steady state photoluminescence (PL) spectra ($\lambda_{\text{ex}} = 375$ nm) and (c) photoluminescence quantum yield (PL QY) of free-standing films of PNCs at different PMMA (40 mg, black line and symbol, 80 mg, red line and symbol, 140 mg, blue line and symbol) and fixed NCs loading (0.04 mmol) compared to that of CsPbBr₃ NC thin film prepared by spin coating (yellow line and symbol) (d) Time-resolved PL decay curves of PMMA free-standing films and bare NCs thin film.

In Figure 2b–d a detailed spectrofluorimetric characterization, including steady state emission (Figure 2b), PL QY (Figure 2c) and TRPL decays (Figure 2d) of the freestanding films obtained at different PMMA loading is reported and compared with the emission features of bare CsPbBr₃ NCs deposited in thin film (Figure 2, yellow trace).

The comparison of the PL characteristics of these two sets of samples is able to provide significant insights on the NCs behavior, minimizing the contribution due to the different refractive index of the medium surrounding the NCs and of the films thickness. Indeed, the analysis of the PL characteristics of the CsPbBr₃ NCs (i.e., position of the PL band, QY, PL linewidth and decay.) can be conveniently rationalized considering the changes in NC morphologies and/or the yield of radiative/non-radiative recombination processes, dependent on the size and surface passivation of the NCs. The spectrum of

the free-standing film prepared using PMMA 40 mg (Figure 2b, black line) shows an almost symmetric PL band, with a peak wavelength, at 508 nm (2.44 eV), and a FWHM (110 meV) comparable with the NC thin film spectrum in absence of polymer (Figure 2b yellow line, PL band centered at 509 nm and FWHM 115 meV). Conversely, at increasing PMMA loading, the PL band (Figure 2b, red and blue line) moves to longer wavelengths, the FWHM narrows (98 and 100 meV, respectively) and an overall quenching of the absolute PL QY (Figure 2c) is detected. In particular, the free-standing film prepared by using PMMA 40 mg (Figure 2c black circle symbol) has an absolute PL QY of 48%, only slightly lower than that measured for CsPbBr₃ NC thin film (PL QY 55%), but that decreases significantly down to 33% and 31% at PMMA load of 80 mg and 140 mg (Figure 2c red and blue circle symbol), respectively. Moreover, a shift of the color point coordinates in the CIE diagrams from the blue region towards the green region is measured (Figure S3c).

The modification of the PL properties of the NCs induced by PMMA load can be discussed by considering heterogeneous phase segregation phenomena [23], which, in general, are correlated to the affinity between the polymer molecular structure and the NC surface chemistry and to the polymer-to-NCs molar ratio. The difference in polarity between the partially hydrophilic PMMA, characterized by acrylates functionalities, and CsPbBr₃ NCs, exposing OA/OAM alkyl chains, is expected to induce phase segregation phenomena, which makes the NCs to assemble into multiparticle nanostructures within the polymer matrix. The occurrence of such phase segregated structures may reasonably affect the NCs PL, due to possible energy transfer phenomena between NCs in close proximity. However, since the PL spectral features remain overall unchanged for free-standing film prepared at the lowest tested PMMA loading, under this preparative condition, segregation phenomena can be thought to be limited. Such hypothesis is confirmed by the TEM characterization of the corresponding PNC film spin-coated on the TEM grid (see Figure S3A) that reveals well separated NCs, distributed over a large area, and only a small number of NCs forming close packed assemblies. In free standing films at higher PMMA load (80 mg and 140 mg) the NC emission band red shift and its concomitant quenching (Figure 2b,c) cannot be only ascribed to the different dielectric constant experienced by the NCs in presence of the polymer matrix, as such an effect is negligible at PMMA 40 mg load. However, NCs phase segregation, hence their partial aggregation, as also confirmed by TEM investigation (See Figure S3b), should be considered. This can be explained by an unfavorable PMMA: NCs molar ratio, and thus an ultimate imbalance of the hydrophilic acrylate functionalities and the hydrophobic NCs surface terminating chains, which leads to aggregation phenomena in the polymer matrix.

PL decay of the CsPbBr₃ NC spin coated thin film (Figure 2d, yellow line) and the free-standing films prepared with PMMA 40 mg (Figure 2d black line) and 80 mg (Figure 2d red line) were measured by TCSPC to determine the recombination dynamics of excitons in the perovskite NC film. The decay curves can be best fitted with triexponential decay functions and the corresponding average PL lifetimes (τ_{avg}) are reported in Figure 2d (See also Table in Figure S4) and listed in the Table in Figure 3.

$$\tau_r = \frac{\tau_{average}}{PL\ QY} k_r = \frac{1}{\tau_r} k_{nr} = \frac{1}{\tau_{average}} - k_r$$

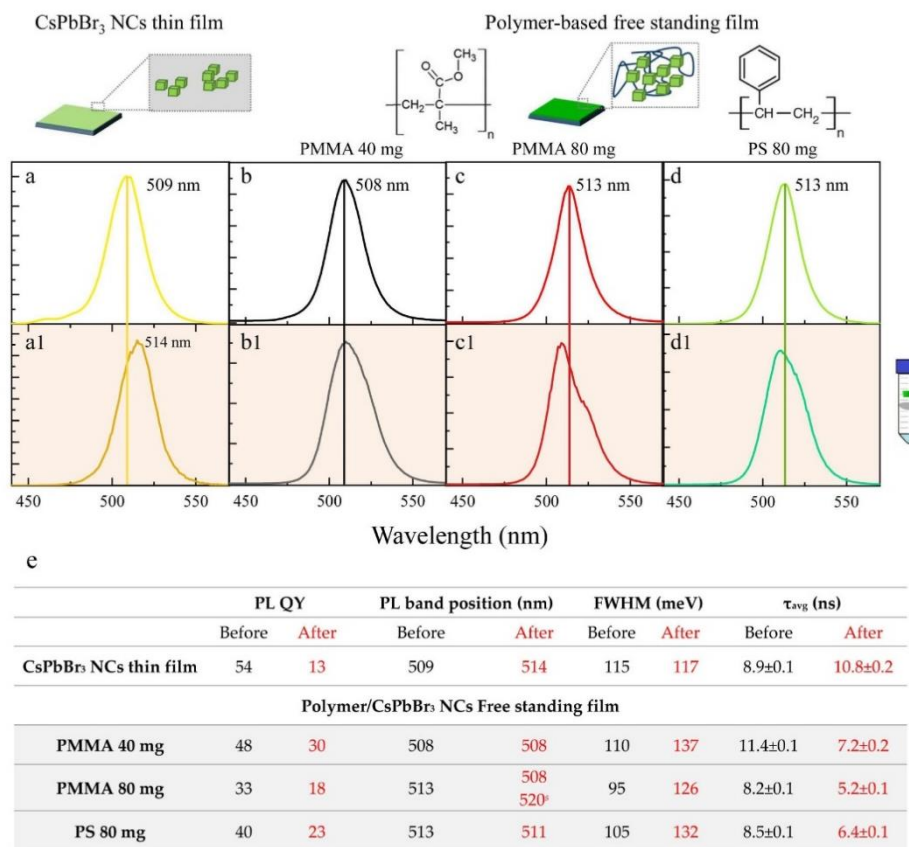


Figure 3. Steady-state fluorescent spectra ($\lambda_{ex} = 375$ nm) of NCs thin film (a,a1) and free-standing films prepared at PMMA 40 mg (b,b1), 80 mg (c,c1) and PS 80 mg (d,d1) and fixed CsPbBr₃ loading (0.04 mmol), before (a–d) and after (a1–d1) 280 h exposure to air and moisture. The table in panel e summarizes the main fluorescence (PL) features: PL quantum yield (PL QY), emission band position, full width at half maximum (FWHM), average lifetimes τ_{avg} . Upper panels: sketches of the CsPbBr₃ NCs deposited as thin film (left) and embedded in a polymer matrix (right).

While the film prepared at PMMA 40 mg shows a τ_{avg} of nearly 11.4 ns, larger than that calculated for NCs thin films (8.9 ns), a shortening of the τ_{avg} to nearly 8.2 ns is measured at higher PMMA load (80 mg). The polymeric matrix embedding the perovskite NCs then affects the NC recombination dynamics and, accordingly the exciton lifetime, as a consequence of possible modifications in surface passivation or energy transfer phenomena between the close packed NCs, phase segregated within the polymer matrix [7,42,45].

To elucidate such effect, the kinetic model describing the relaxation processes of charge carriers and the radiative and non-radiative recombination rates can be exploited. The radiative recombination lifetime (τ_{avg}) and radiative (k_r) and nonradiative (k_{nr}) decay rates were calculated based on the τ_{avg} and on the measured values of PL QY using the equations reported in Table 1.

Table 1. Radiative lifetimes (τ_r), radiative (k_r) and nonradiative (k_{nr}) recombination rates, calculated for CsPbBr₃ NCs thin film and PMMA- (40 mg and 80 mg load) and PS- (80 mg load) based free standing films before (values in black) and after (values in red) 280 h exposure to relative humidity RH% = 85–90% at 25 °C.

	τ_r (ns)		k_r (ns ⁻¹)		k_{nr} (ns ⁻¹)	
	Before	After	Before	After	Before	After
NC thin film	17	83	0.061	0.012	0.052	0.080
PMMA 40 mg	24	24	0.042	0.042	0.045	0.097
PMMA 80 mg	25	24	0.040	0.042	0.082	0.150
PS 80 mg	21	28	0.047	0.036	0.071	0.120

It is worth noticing that the values of τ_r increases markedly from 17 ns, for NC thin film, to 24 (25) ns for PMMA 40 mg (80 mg) free standing films, thus suggesting a more efficient passivation provided by the polymer to the NCs.

Notably, the k_{nr} decreases from 0.052 ns⁻¹ for NC thin film to 0.045 ns⁻¹ for PMMA 40 mg free-standing film, indicating a reduction of the possible non-radiative pathways due to the presence of the polymer. Instead, an increase in the k_{nr} at 0.082 ns⁻¹ is calculated at 80 mg PMMA load. Considering the red shift of the emission band and the significant decrease of the PL QY and of the τ_{avg} , the results can be related to reabsorption or energy transfer mechanisms between NCs having different size hence different bandgap, considering that, at this polymer load, NCs segregate in multiple assemblies.

To test the moisture/air resistance of CsPbBr₃ NCs in the different fabricated films, they were exposed to KNO₃ saturated water solution in a closed chamber filled with air (See Materials and methods section), monitoring the time course of the emission properties. Figure 3 compares the steady-state fluorescence before (Figure 3a–c) and after (Figure 3(a1)–(c1)) 280 h of air and moisture exposure of the NCs thin film (Figure 3a,(a1)) and free-standing films prepared using PMMA 40 mg (Figure 3b,(b1)), PMMA 80 mg (Figure 3c,(c1)) along with a table (Figure 3e) summarizing the value of the PL features, including PL QY, emission band position, FWHM, and average lifetimes τ_{avg} . To get insight on the moisture uptake phenomenon, PS based nanocomposites were also prepared, as PS is characterized by a lower percentage of water absorption (0.05) and reduced moisture permeability (0.8–3.9 g mm/m² day) than PMMA. Therefore, free-standing PS (80 mg) films were prepared and characterized (Figure 3d,(d1)) and their properties compared to those of PMMA one (Figure 3c,(c1)). After moisture/air exposure, the NC thin film (Figure 3a,(a1)) shows still a symmetric, though red shifted, emission band, at 514 nm, with a PL QY of only 13% (Figure 3e), significantly lower than the initial value of 54%. Less marked PL quenching upon moisture/air exposure is detected for the free-standing film, and PL QY value of 30% (Δ PL QY = 18) and 18% (Δ PL QY = 15) are found (Figure 3e) for samples prepared with 40 mg and 80 mg PMMA, respectively. The emission peak (Figure 3(b1),(c1)) after moisture exposure is still at 508 nm for the free-standing film prepared with 40 mg PMMA (Figure 3(b1),e) though broadened (FWHM = 137 meV) and asymmetric, presenting a shoulder on the low energy side. Instead, PL signal of 80 mg PMMA free-standing film blue shifts, showing an intense peak at nearly 508 nm and the presence of a shoulder at nearly 520 nm (Figure 3(c1)). To elucidate the impact of the environmental conditions on NC thin film and PMMA based free-standing films, recombination dynamics were investigated and PL lifetimes (Figure 3e), radiative recombination lifetimes and radiative and non-radiative decay rates (Table 1) calculated.

The red shift of the emission (from 508 nm to 514 nm) measured for NC thin film after humidity exposure, together with the longer τ_{avg} (from 8.9 ns to 10.8 ns) and the increased τ_r (from 17 ns to 83 ns) can be attributed to a slight increase in size of the NCs [42,45]. Meanwhile, the higher k_{nr} value, ascribed to increased nonradiative recombination pathways, suggests a higher density of surface trap states. Taking into account the dynamic binding of ligands at the NC surface, the ionic nature of crystals and the low energy of formation of the perovskite NCs, a degradation process induced by moisture/air exposure can be considered, which involves ligand molecules detachment and recrystallization.

The partial removal of ligands, upon humidity exposure, may promote aggregation/recrystallization of NCs, which are confined in the restrained volume of the film, resulting in the evolution towards slightly larger and poorly passivated NCs.

Regardless of the PMMA load, free-standing films show recombination dynamics faster than what found in the NCs thin film, thus suggesting a different moisture induced degradation of the NCs when they are embedded in the polymer. In particular, τ_{avg} decreases down to few ns (Figure 3e), with τ_r and k_r remaining unchanged (Table 1) and k_{nr} drastically increases up to 0.095 ns^{-1} and 0.150 ns^{-1} for the 40 mg and 80 mg PMMA films, respectively. The preserved values of τ_r and k_r for free-standing films suggest a large fraction of NCs retaining their size even after 280 h of moisture exposure [42,45]. The limited influence of the NC aggregation in these samples is also pointed out by the almost negligible red shift of the emission band (Figure 3(b1),(c1) versus Figure 2b,c). However, considering the evolution of the emission band shape upon moisture exposure as a function of PMMA load (Figure 3(b1),(c1) versus Figure 3b,c), the role played by the amount of PMMA in the NC degradation must also be considered. In particular, while the 40 mg PMMA film shows a broader emission band with additional components at lower energy, the 80 mg PMMA film displays a structured emission band, with a main, blue shifted peak at 508 nm and a shoulder at 520 nm. Such a latter change in the emission band shape can be explained by taking into account moisture-induced (i) polymer swelling, which could, in principle, affect the NC assembly within the polymer, and/or (ii) dismantling of NCs as a consequence of their intrinsic structural instability. It is well noted [36] that relatively thin PMMA films (here 30 and 40 μm , for 40 mg and 80 mg PMMA free-standing film, respectively) undergo plasticization and hygroscopic swelling following exposure to moisture, and the extent of such a swelling has been shown to depend on the density of the hydrophilic groups. It turns out that a more prominent swelling would be expected for the 80 mg PMMA film rather than in the 40 mg counterpart, due to the larger number of hydrophilic acrylate functionalities. Therefore, upon moisture exposure, NCs phase segregated in the 80 mg PMMA film can be pushed far apart from each other as the polymer swells. Consequently, the emission band shows a more intense component at 508 nm, which is the emission wavelength characteristic of the pristine NCs in solid films, and a weaker component at lower energy, ascribed to energy transfer phenomena among closely packed NCs that are, however, still present, though to a lower extent. Indeed, it cannot be excluded that such an increase in emission intensity at higher energy could be also due to moisture-induced dismantling of larger size NC, much more evident for 80 mg PMMA film because of the higher extent of moisture uptake. This hypothesis also corroborates the longer k_{nr} calculated for this sample: a higher density of surface trap states, and thus an increase in the non-radiative recombination rate, are in line with the NC size decreases, which turns in a higher surface-to-volume ratio. The moisture-induced ligand detachment that leads to less passivated NCs and to non-radiative recombination pathways, could also contribute to the higher k_{nr} value calculated for the PMMA based films.

Compared to PMMA films, the PS counterpart is expected to provide a lower water uptake, because of its hydrophobicity, and thus be able, in principle, to limit the detrimental NC exposure to moisture. Although PS has a higher affinity, in terms of polarity, with the hydrophobic chains of OA/OAM molecules capping CsPbBr₃ NCs, than PMMA, the rigidity of the PS structure [25], due to the aromatic ring, limits the dispersibility of the NCs within the polymer matrix. In fact, morphological (Figure S3d) and spectroscopic (Figure 3d,(d1)) investigation clearly highlight the occurrence of phase segregation. The phenomenon turns in an emission band (Figure 3d green line, FWHM = 105 meV), at 513 nm (2.42 eV), slightly red shifted compared to that displayed by bare NCs film (Figure 3a yellow line), and a lower PL QY of nearly 40%, (Figure 3e) reasonably accounted for by energy/charge transfer phenomena arising from NC phase segregated structures, and/or to the different refractive index, polarity, and film thickness experienced by the NCs within the PS matrix. Interestingly, although PS would be expected to block moisture diffusion compared to PMMA, the spectroscopic characterization (Figure 3) and recombination dynamic investigation (Table 1) of 80 mg PS films exposed to moisture do not evidence a significant improvement of NC stability. Therefore, though less permeable to water,

PS polymer matrix allows a moisture uptake anyway sufficient to induce NC degradation. On the other hand, the limited swelling of the polymer, due to its hydrophobic character, results in an almost preserved emission band shape, which only slightly blue shifts and broadens.

Direct comparison between the here attained results and literature reported data is difficult due to the huge number of polymer-based stabilization methods reported in literature for perovskites [46–48], differing in the nanocrystals synthetic step, approach used for the nanocomposite preparation (*ex situ* or *in situ*), and moisture condition tested. The data here shown partially confirm those reported by others works, based on *ex situ* nanocomposite preparation and CsPbBr₃ synthesized by hot-injection strategy. However, the adding value that the systematic and fundamental investigation here performed wants to offer to the general discussion regarding the IP NC stability is the in-depth description of the processes involving the NCs within a polymer matrix, which depend on the polymer loading, nature/swelling properties, together with the quantitative evaluation of the benefit provided by the polymer, as estimated by the spectroscopic characterization.

4. Conclusions

An *ex situ* approach has been successfully developed for the easy fabrication of free-standing films composed by CsPbBr₃ NCs and high molecular weight PMMA or PS polymer, in order to evaluate the effect of the polymer matrix on blocking moisture diffusion and, hence on the long term stability of the NCs. The fluorescent properties of the films, including steady state emission, PL average lifetimes and recombination dynamics, have been thoroughly investigated and discussed in terms of polymer structure and load. The polymer efficacy to behave as a moisture barrier has been also considered, comparing the results with those attained for NCs spin coated thin film, used as a reference.

The partial hydrophilicity of PMMA, due to acrylates functionalities, and the hydrophobicity of organic-capped CsPbBr₃ NCs have been considered. The results demonstrated that an adequate molar ratio between polymer and NCs, balancing the hydrophilic and hydrophobic components in the nanocomposite systems, is required to retain NC spectroscopic features in the PNC. An unchanged steady NC emission wavelength, a high radiative and low non-radiative recombination rate were found for 40 mg PMMA load, thus suggesting that the polymer can partially stabilize the NCs. Conversely, NC phase segregation phenomena have been found to take place as PMMA load increases, resulting in an emission band red shift and an increase of non-radiative recombination rates, probably ascribed to energy transfer phenomena. Upon moisture exposure, NCs, while undergoing aggregation when deposited as thin film, have been demonstrated to retain their size upon incorporation in the polymer matrix. However, ligands detachment and increase in surface defects and trap states, as a consequence of the nanocomposite formation, could not be avoided, thus contributing to decrease the PL QY, though to a lower extent than when deposited as thin film. Spectroscopic and morphologic characterizations of free-standing films prepared with highly hydrophobic PS have highlighted phase segregation phenomena ascribed to polymer rigidity due to the aromatic ring in the polymer structure. Though less permeable to water, PS free-standing-film has demonstrated to uptake moisture enough to induce a partial degradation of the NCs.

This study has contributed to the analysis of the effects and the viability of the IP NC encapsulation in polymer as a strategy to limit the water vapour diffusion, crucial for the fabrication of IP NCs based devices. The advantages and the limitations of the presented approach have been highlighted, thus fostering future research to enhance the effectiveness of the encapsulation procedures and exploration of alternative routes.

Supplementary Materials: The following are available online at <http://www.mdpi.com/1996-1073/13/24/6730/s1>, Figure S1: statistical analysis of the size distribution of as synthesized CsPbBr₃ nanocrystals; Figure S2: Sketch of the nanocomposite blend processing in free-standing films; Figure S3: TEM micrographs of nanocomposites at different polymer loading and color point position in the CIE 1931 diagram of PMMA-based free-standing films; Figure S4: Time resolved photoluminescence decay of CsPbBr₃ NC thin spin coated film and free-standing films and fitting parameters before and after moisture exposure.

Author Contributions: Conceptualization, E.F. and M.S.; methodology, E.F., R.S., A.P., and A.M.L.; formal analysis, E.F., A.P., M.S., and A.M.L.; investigation, E.F., R.S., and A.P.; resources, M.S. and M.L.C. data curation, E.F., R.S., A.P., and N.D.; writing—original draft preparation, E.F., A.P., N.D., M.L.C., and M.S.; writing—review and editing, E.F., A.P., N.D., A.A., M.L.C., and M.S.; visualization, E.F., R.S., A.P., M.L.C., and M.S.; supervision, E.F., M.S., and A.P.; funding acquisition, A.A., M.S., and M.L.C. All authors have read and agreed to the published version of the manuscript.

Funding: The work has been funded by the Italian PON Project ARS01_00519 “BEST-4U”.

Acknowledgments: The authors gratefully thank G. Palazzo, Department of Chemistry, University of Bari, for the help and discussion regarding the set up for moisture exposure experiments.

Conflicts of Interest: The authors declare no conflict of interest.

References

1. Kovalenko, M.V.; Protesescu, L.; Bodnarchuk, M.I. Properties and potential optoelectronic applications of lead halide perovskite nanocrystals. *Science* **2017**, *358*, 745. [[CrossRef](#)]
2. Brennan, M.C.; Zinna, J.; Kuno, M. Existence of a Size-Dependent Stokes Shift in CsPbBr₃ Perovskite Nanocrystals. *ACS Energy Lett.* **2017**, *2*, 1487–1488. [[CrossRef](#)]
3. Grisorio, R.; Fanizza, E.; Allegretta, I.; Altamura, D.; Striccoli, M.; Terzano, R.; Giannini, C.; Vergaro, V.; Ciccarella, G.; Margiotta, N.; et al. Insights into the role of the lead/surfactant ratio in the formation and passivation of cesium lead bromide perovskite nanocrystals. *Nanoscale* **2020**, *12*, 623–637. [[CrossRef](#)] [[PubMed](#)]
4. Grisorio, R.; Conelli, D.; Giannelli, R.; Fanizza, E.; Striccoli, M.; Altamura, D.; Giannini, C.; Allegretta, I.; Terzano, R.; Suranna, G.P. A new route for the shape differentiation of cesium lead bromide perovskite nanocrystals with near-unity photoluminescence quantum yield. *Nanoscale* **2020**, *12*, 17053–17063. [[CrossRef](#)] [[PubMed](#)]
5. El-Ballouli, A.a.O.; Bakr, O.M.; Mohammed, O.F. Compositional, Processing, and Interfacial Engineering of Nanocrystal- and Quantum-Dot-Based Perovskite Solar Cells. *Chem. Mater.* **2019**, *31*, 6387–6411. [[CrossRef](#)]
6. McDonald, C.; Ni, C.; Maguire, P.; Connor, P.; Irvine, J.T.S.; Mariotti, D.; Svrcek, V. Nanostructured Perovskite Solar Cells. *Nanomaterials* **2019**, *9*, 1481. [[CrossRef](#)]
7. Zhao, L.; Yeh, Y.-W.; Tran, N.L.; Wu, F.; Xiao, Z.; Kerner, R.A.; Lin, Y.L.; Scholes, G.D.; Yao, N.; Rand, B.P. In Situ Preparation of Metal Halide Perovskite Nanocrystal Thin Films for Improved Light-Emitting Devices. *ACS Nano* **2017**, *11*, 3957–3964. [[CrossRef](#)]
8. Zhou, Y.; Zhao, Y. Chemical stability and instability of inorganic halide perovskites. *Energy Environ. Sci.* **2019**, *12*, 1495–1511. [[CrossRef](#)]
9. Zheng, X.; Troughton, J.; Gasparini, N.; Lin, Y.; Wei, M.; Hou, Y.; Liu, J.; Song, K.; Chen, Z.; Yang, C.; et al. Quantum Dots Supply Bulk- and Surface-Passivation Agents for Efficient and Stable Perovskite Solar Cells. *Joule* **2019**, *3*, 1963–1976. [[CrossRef](#)]
10. Jena, A.K.; Kulkarni, A.; Miyasaka, T. Halide Perovskite Photovoltaics: Background, Status, and Future Prospects. *Chem. Rev.* **2019**, *119*, 3036–3103. [[CrossRef](#)]
11. Fanizza, E.; Cascella, F.; Altamura, D.; Giannini, C.; Panniello, A.; Triggiani, L.; Panzarea, F.; Depalo, N.; Grisorio, R.; Suranna, G.P.; et al. Post-synthesis phase and shape evolution of CsPbBr₃ colloidal nanocrystals: The role of ligands. *Nano Res.* **2019**, *12*, 1155–1166. [[CrossRef](#)]
12. Kim, B.; Seok, S.I. Molecular aspects of organic cations affecting the humidity stability of perovskites. *Energy Environ. Sci.* **2020**, *13*, 805–820. [[CrossRef](#)]
13. Liu, S.-C.; Li, Z.; Yang, Y.; Wang, X.; Chen, Y.-X.; Xue, D.-J.; Hu, J.-S. Investigation of Oxygen Passivation for High-Performance All-Inorganic Perovskite Solar Cells. *J. Am. Chem. Soc.* **2019**, *141*, 18075–18082. [[CrossRef](#)] [[PubMed](#)]
14. Zhang, Q.; Yin, Y. All-Inorganic Metal Halide Perovskite Nanocrystals: Opportunities and Challenges. *ACS Cent. Sci.* **2018**, *4*, 668–679. [[CrossRef](#)]
15. Raja, S.N.; Bekenstein, Y.; Koc, M.A.; Fischer, S.; Zhang, D.; Lin, L.; Ritchie, R.O.; Yang, P.; Alivisatos, A.P. Encapsulation of Perovskite Nanocrystals into Macroscale Polymer Matrices: Enhanced Stability and Polarization. *ACS Appl. Mater. Interfaces* **2016**, *8*, 35523–35533. [[CrossRef](#)]

16. Tong, J.; Wu, J.; Shen, W.; Zhang, Y.; Liu, Y.; Zhang, T.; Nie, S.; Deng, Z. Direct Hot-Injection Synthesis of Lead Halide Perovskite Nanocubes in Acrylic Monomers for Ultrastable and Bright Nanocrystal–Polymer Composite Films. *ACS Appl. Mater. Interfaces* **2019**, *11*, 9317–9325. [[CrossRef](#)]
17. Hintermayr, V.A.; Lampe, C.; Löw, M.; Roemer, J.; Vanderlinden, W.; Gramlich, M.; Böhm, A.X.; Sattler, C.; Nickel, B.; Lohmüller, T.; et al. Polymer Nanoreactors Shield Perovskite Nanocrystals from Degradation. *Nano Lett.* **2019**, *19*, 4928–4933. [[CrossRef](#)]
18. Li, Z.; Hu, Q.; Tan, Z.; Yang, Y.; Leng, M.; Liu, X.; Ge, C.; Niu, G.; Tang, J. Aqueous Synthesis of Lead Halide Perovskite Nanocrystals with High Water Stability and Bright Photoluminescence. *ACS Appl. Mater. Interfaces* **2018**, *10*, 43915–43922. [[CrossRef](#)]
19. Xuan, T.; Yang, X.; Lou, S.; Huang, J.; Liu, Y.; Yu, J.; Li, H.; Wong, K.-L.; Wang, C.; Wang, J. Highly stable CsPbBr₃ quantum dots coated with alkyl phosphate for white light-emitting diodes. *Nanoscale* **2017**, *9*, 15286–15290. [[CrossRef](#)]
20. Meyns, M.; Perálvarez, M.; Heuer-Jungemann, A.; Hertog, W.; Ibáñez, M.; Nafria, R.; Genç, A.; Arbiol, J.; Kovalenko, M.V.; Carreras, J.; et al. Polymer-Enhanced Stability of Inorganic Perovskite Nanocrystals and Their Application in Color Conversion LEDs. *ACS Appl. Mater. Interfaces* **2016**, *8*, 19579–19586. [[CrossRef](#)]
21. Li, R.; Wei, Z.; Zhao, H.; Yu, H.; Fang, X.; Fang, D.; Li, J.; He, T.; Chen, R.; Wang, X. Linear and nonlinear optical characteristics of all-inorganic perovskite CsPbBr₃ quantum dots modified by hydrophobic zeolites. *Nanoscale* **2018**, *10*, 22766–22774. [[CrossRef](#)] [[PubMed](#)]
22. Li, X.; Xue, Z.; Luo, D.; Huang, C.; Liu, L.; Qiao, X.; Liu, C.; Song, Q.; Yan, C.; Li, Y.; et al. A stable lead halide perovskite nanocrystals protected by PMMA. *Sci. China Mater.* **2018**, *61*, 363–370. [[CrossRef](#)]
23. Xin, Y.; Zhao, H.; Zhang, J. Highly Stable and Luminescent Perovskite–Polymer Composites from a Convenient and Universal Strategy. *ACS Appl. Mater. Interfaces* **2018**, *10*, 4971–4980. [[CrossRef](#)] [[PubMed](#)]
24. Liao, H.; Guo, S.; Cao, S.; Wang, L.; Gao, F.; Yang, Z.; Zheng, J.; Yang, W. A General Strategy for In Situ Growth of All-Inorganic CsPbX₃ (X = Br, I, and Cl) Perovskite Nanocrystals in Polymer Fibers toward Significantly Enhanced Water/Thermal Stabilities. *Adv. Opt. Mater.* **2018**, *6*, 1800346. [[CrossRef](#)]
25. Rainò, G.; Landuyt, A.; Krieg, F.; Bernasconi, C.; Ochsenbein, S.T.; Dirin, D.N.; Bodnarchuk, M.I.; Kovalenko, M.V. Underestimated Effect of a Polymer Matrix on the Light Emission of Single CsPbBr₃ Nanocrystals. *Nano Lett.* **2019**, *19*, 3648–3653. [[CrossRef](#)]
26. Song, Y.H.; Yoo, J.S.; Kang, B.K.; Choi, S.H.; Ji, E.K.; Jung, H.S.; Yoon, D.H. Long-term stable stacked CsPbBr₃ quantum dot films for highly efficient white light generation in LEDs. *Nanoscale* **2016**, *8*, 19523–19526. [[CrossRef](#)]
27. Xuan, T.; Huang, J.; Liu, H.; Lou, S.; Cao, L.; Gan, W.; Liu, R.-S.; Wang, J. Super-Hydrophobic Cesium Lead Halide Perovskite Quantum Dot-Polymer Composites with High Stability and Luminescent Efficiency for Wide Color Gamut White Light-Emitting Diodes. *Chem. Mater.* **2019**, *31*, 1042–1047. [[CrossRef](#)]
28. Li, Z.; Kong, L.; Huang, S.; Li, L. Highly Luminescent and Ultrastable CsPbBr₃ Perovskite Quantum Dots Incorporated into a Silica/Alumina Monolith. *Angew. Chem. Int. Ed.* **2017**, *56*, 8134–8138. [[CrossRef](#)]
29. Xiang, Q.; Zhou, B.; Cao, K.; Wen, Y.; Li, Y.; Wang, Z.; Jiang, C.; Shan, B.; Chen, R. Bottom up Stabilization of CsPbBr₃ Quantum Dots-Silica Sphere with Selective Surface Passivation via Atomic Layer Deposition. *Chem. Mater.* **2018**, *30*, 8486–8494. [[CrossRef](#)]
30. Song, W.; Wang, Y.; Wang, B.; Yao, Y.; Wang, W.; Wu, J.; Shen, Q.; Luo, W.; Zou, Z. Super stable CsPbBr₃@SiO₂ tumor imaging reagent by stress-response encapsulation. *Nano Res.* **2020**, *13*, 795–801. [[CrossRef](#)]
31. Sun, C.; Zhang, Y.; Ruan, C.; Yin, C.; Wang, X.; Wang, Y.; Yu, W.W. Efficient and Stable White LEDs with Silica-Coated Inorganic Perovskite Quantum Dots. *Adv. Mater.* **2016**, *28*, 10088–10094. [[CrossRef](#)] [[PubMed](#)]
32. Li, Z.; Liu, X.; Xu, J.; Yang, S.; Zhao, H.; Huang, H.; Liu, S.F.; Yao, J. 2D–3D Cs₂PbI₂Cl₂–CsPbI_{2.5}Br_{0.5} Mixed-Dimensional Films for All-Inorganic Perovskite Solar Cells with Enhanced Efficiency and Stability. *J. Phys. Chem. Lett.* **2020**, *11*, 4138–4146. [[CrossRef](#)] [[PubMed](#)]
33. Lou, S.; Zhou, Z.; Xuan, T.; Li, H.; Jiao, J.; Zhang, H.; Gautier, R.; Wang, J. Chemical Transformation of Lead Halide Perovskite into Insoluble, Less Cytotoxic, and Brightly Luminescent CsPbBr₃/CsPb₂Br₅ Composite Nanocrystals for Cell Imaging. *ACS Appl. Mater. Interfaces* **2019**, *11*, 24241–24246. [[CrossRef](#)] [[PubMed](#)]
34. Wang, X.; Lian, X.; Zhang, Z.; Gao, H. Could Nanocomposites Continue the Success of Halide Perovskites? *ACS Energy Lett.* **2019**, *4*, 1446–1454. [[CrossRef](#)]

35. Ingrosso, C.; Panniello, A.; Comparelli, R.; Curri, M.L.; Striccoli, M. Colloidal Inorganic Nanocrystal Based Nanocomposites: Functional Materials for Micro and Nanofabrication. *Materials* **2010**, *3*, 1316–1352. [[CrossRef](#)]
36. Nolte, A.J.; Treat, N.D.; Cohen, R.E.; Rubner, M.F. Effect of Relative Humidity on the Young's Modulus of Polyelectrolyte Multilayer Films and Related Nonionic Polymers. *Macromolecules* **2008**, *41*, 5793–5798. [[CrossRef](#)]
37. Xu, J.; Li, D. Preparation and Photoluminescence of Transparent Poly(methyl methacrylate)-Based Nanocomposite Films with Ultra-High-Loading Pendant ZnS Quantum Dots. *Polymers* **2018**, *10*, 1217. [[CrossRef](#)]
38. Ismail, R.A.; Almashhadani, N.J.; Sadik, R.H. Preparation and properties of polystyrene incorporated with gold and silver nanoparticles for optoelectronic applications. *Appl. Nanosci.* **2017**, *7*, 109–116. [[CrossRef](#)]
39. Maes, J.; Balcaen, L.; Drijvers, E.; Zhao, Q.; De Roo, J.; Vantomme, A.; Vanhaecke, F.; Geiregat, P.; Hens, Z. Light Absorption Coefficient of CsPbBr₃ Perovskite Nanocrystals. *J. Phys. Chem. Lett.* **2018**, *9*, 3093–3097. [[CrossRef](#)]
40. Cheng, O.H.-C.; Qiao, T.; Sheldon, M.; Son, D.H. Size- and temperature-dependent photoluminescence spectra of strongly confined CsPbBr₃ quantum dots. *Nanoscale* **2020**, *12*, 13113–13118. [[CrossRef](#)]
41. Butkus, J.; Vashishtha, P.; Chen, K.; Gallaher, J.K.; Prasad, S.K.K.; Metin, D.Z.; Laufersky, G.; Gaston, N.; Halpert, J.E.; Hodgkiss, J.M. The Evolution of Quantum Confinement in CsPbBr₃ Perovskite Nanocrystals. *Chem. Mater.* **2017**, *29*, 3644–3652. [[CrossRef](#)]
42. Li, G.; Huang, J.; Zhu, H.; Li, Y.; Tang, J.-X.; Jiang, Y. Surface Ligand Engineering for Near-Unity Quantum Yield Inorganic Halide Perovskite QDs and High-Performance QLEDs. *Chem. Mater.* **2018**, *30*, 6099–6107. [[CrossRef](#)]
43. Imran, M.; Ijaz, P.; Baranov, D.; Goldoni, L.; Petralanda, U.; Akkerman, Q.; Abdelhady, A.L.; Prato, M.; Bianchini, P.; Infante, I.; et al. Shape-Pure, Nearly Monodispersed CsPbBr₃ Nanocubes Prepared Using Secondary Aliphatic Amines. *Nano Lett.* **2018**, *18*, 7822–7831. [[CrossRef](#)] [[PubMed](#)]
44. Panniello, A.; Di Mauro, A.E.; Fanizza, E.; Depalo, N.; Agostiano, A.; Curri, M.L.; Striccoli, M. Luminescent Oil-Soluble Carbon Dots toward White Light Emission: A Spectroscopic Study. *J. Phys. Chem. C* **2018**, *122*, 839–849. [[CrossRef](#)]
45. Naghadeh, S.B.; Luo, B.; Pu, Y.-C.; Schwartz, Z.; Hollingsworth, W.R.; Lindley, S.A.; Brewer, A.S.; Ayzner, A.L.; Zhang, J.Z. Size Dependence of Charge Carrier Dynamics in Organometal Halide Perovskite Nanocrystals: Deciphering Radiative Versus Nonradiative Components. *J. Phys. Chem. C* **2019**, *123*, 4610–4619. [[CrossRef](#)]
46. Shangguan, Z.; Zheng, X.; Zhang, J.; Lin, W.; Guo, W.; Li, C.; Wu, T.; Lin, Y.; Chen, Z. The Stability of Metal Halide Perovskite Nanocrystals—A Key Issue for the Application on Quantum-Dot-Based Micro Light-Emitting Diodes Display. *Nanomaterials* **2020**, *10*, 1375. [[CrossRef](#)]
47. Liu, M.; Matuhina, A.; Zhang, H.; Vivo, P. Advances in the Stability of Halide Perovskite Nanocrystals. *Materials* **2019**, *12*, 3733. [[CrossRef](#)]
48. Lou, S.; Xuan, T.; Wang, J. (INVITED) Stability: A desiderated problem for the lead halide perovskites. *Opt. Mater. X* **2019**, *1*, 100023. [[CrossRef](#)]

Publisher's Note: MDPI stays neutral with regard to jurisdictional claims in published maps and institutional affiliations.



© 2020 by the authors. Licensee MDPI, Basel, Switzerland. This article is an open access article distributed under the terms and conditions of the Creative Commons Attribution (CC BY) license (<http://creativecommons.org/licenses/by/4.0/>).